Energy-Resolved Femtosecond Hot Electron Dynamics in Single Plasmonic Nanoparticles

Jacob Pettine, Paolo Maioli, Fabrice Vallée, Natalia del Fatti, David Nesbitt

▶ **To cite this version:**

Jacob Pettine, Paolo Maioli, Fabrice Vallée, Natalia del Fatti, David Nesbitt. Energy-Resolved Femtosecond Hot Electron Dynamics in Single Plasmonic Nanoparticles. ACS Nano, 2023, 17 (11), pp.10721-10732. 10.1021/acsnano.3c02062 . hal-04146050

HAL Id: hal-04146050
https://hal.science/hal-04146050

Submitted on 7 Sep 2023

HAL is a multi-disciplinary open access archive for the deposit and dissemination of scientific research documents, whether they are published or not. The documents may come from teaching and research institutions in France or abroad, or from public or private research centers.

L'archive ouverte pluridisciplinaire **HAL**, est destinée au dépôt et à la diffusion de documents scientifiques de niveau recherche, publiés ou non, émanant des établissements d'enseignement et de recherche français ou étrangers, des laboratoires publics ou privés.

Energy-Resolved Femtosecond Hot Electron Dynamics in Single Plasmonic Nanoparticles

Jacob Pettine,[1,2,3 *] Paolo Maioli,[4] Fabrice Vallee,[4] Natalia Del Fatti,[4,5] and David J. Nesbitt[1,2,6 *]

[1] JILA, University of Colorado Boulder and the National Institute of Standards and Technology, Boulder, Colorado 80309, United States

[2] Department of Physics, University of Colorado Boulder, Boulder, Colorado 80309, United States

[3] Center for Integrated Nanotechnologies, Los Alamos National Laboratory, Los Alamos, NM 87545, United States

[4] Université de Lyon, CNRS, Université Claude Bernard Lyon 1, Institut Lumière Matière, 69622 Villeurbanne Cedex, France

[5] Institut Universitaire de France (IUF), France

[6] Department of Chemistry, University of Colorado Boulder, Boulder, Colorado 80309, United States

[*] *Correspondence may be addressed to J.P. (jacob.pettine@lanl.gov) or D.J.N. (djn@jila.colorado.edu)*

Abstract

Efficient excitation and harvesting of hot carriers from nanoscale metals is central to many emerging photochemical, photovoltaic, and ultrafast optoelectronic applications. Yet direct experimental evidence of the energy-dependent femtosecond dynamics in ubiquitous tens-of-nanometer gold structures remains elusive, despite the potentially rich interplay between interfacial and internal plasmonic fields, excitation distributions, and scattering processes. To explore the effects of nanoscale structure on these dynamics, we employ a new technique for simultaneous time-, angle-, and energy-resolved photoemission spectroscopy of single plasmonic nanoparticles. Photoelectron velocity and electric field distributions reveal bulk-like ballistic hot electron transport in different geometries, lacking any signatures of surface effects. Energy-resolved dynamics are measured in the 1–2 eV range and extrapolated to lower energies via Boltzmann theory, providing a detailed view of hot electron lifetimes within nanoscale gold. We find that particles with relevant dimensions as small as 10 nm serve as exemplary platforms for studying intrinsic metal dynamics.

Keywords: *hot electrons, ballistic dynamics, angle-resolved, photoemission spectroscopy, single-particle, Monte Carlo, Boltzmann theory*

Plasmonic oscillations in metal nanoparticles generate strong, nanolocalized optical field enhancements and high densities of photoexcited electrons and holes. Whether nascent (nonthermal) or internally thermalized via electron-electron scattering, such excitations are often referred to as "hot" charge carriers, with average optical excitation energies much greater than the thermal energy of the metal lattice, $k_B T_l$. Efficient harvesting of these hot carriers is critical for a broad range of emerging applications, including plasmon-enhanced photocatalysis,[1-3] solar photovoltaics,[4-6] biotherapeutics,[7] and ultrafast integrated photodetection.[8, 9] However, the ability to tailor nanoplasmonic systems for optimized hot carrier collection efficiencies remains an ongoing challenge, requiring detailed knowledge of energy-dependent femtosecond hot carrier lifetimes and their nanoscale geometry-dependent spatial and vector momentum distributions. Ballistic carrier collection efficiencies, in particular, are often well below 1%.[6, 10, 11]

Energy-averaged hot carrier thermalization kinetics have been well studied in metal nanoparticles using ultrafast optical pump-probe measurements of the transient dielectric response.[12-15] Such studies have been central to understanding picosecond electron-lattice thermalization and impulsive acoustic excitations,[16-18] also offering insight into hundreds-of-femtosecond electron-electron thermalization times.[19] However, the overall energy-averaged response probed in these studies is disproportionately influenced by the longer lifetimes ($>$ 100 fs) of lower-energy hot carriers ($<$ 1 eV), masking the much faster tens-of-femtosecond decay times of the higher-energy nascent carriers. It is these nascent carriers that are most relevant for applications involving charge emission over interfacial barriers (e.g., $\sim$1.1 eV for an Au-TiO_2 interface[2, 4]) and transfer into admolecular surface states. The nascent carrier distribution contains orders of magnitude greater available energy than the thermalized distributions above 1 eV, even at 1000 K thermalized electron temperatures.[20] Energy-resolved studies are therefore needed to directly characterize the faster ($<$ 100 fs) lifetimes on which these high-energy nascent carriers must be extracted.

Energy-resolved two-photon photoemission (2PPE) has been commonly utilized to probe hot carrier dynamics in bulk and thin film metal systems,[21-23] while studies of femtosecond carrier lifetimes in metal nanoparticles remain relatively limited. Stimulated by initial investigations of nanoparticle ensembles,[24-26] nanoscale photoemission capabilities have steadily evolved over the past couple decades, with nanometer-scale photoemission hot spots,[27, 28] few-femtosecond plasmon dephasing dynamics,[29, 30] energy-dependent lifetime trends,[31, 32] and

photoelectron momentum distributions[33-37] all measured at the single nanoparticle level. Complementary progress has been made in theoretically modeling photoelectron spatial and momentum distributions in arbitrary nanoscale geometries.[35, 38-40] Despite these advances, the direct characterization of energy-dependent hot carrier lifetimes in nanostructured gold has been critically overlooked, while an even more pressing need for time- and angle-resolved dynamical insights into the correspondence between nanoscale geometry, spatial excitation density, and carrier momentum distributions has eluded experiment. The unambiguous interpretation of angle-resolved photoemission spectra demands single-nanoparticle resolution, which also serves to elucidate behaviors that vary or remain consistent from particle to particle in the presence of defects, orientational effects, resonance shifts, and inter-particle coupling.

To help address these problems, we combine ultrafast pump-probe excitation, scanning photoemission microscopy, and velocity-resolved detection methods to view the femtosecond hot electron dynamics within single, well-characterized gold nanoparticles. The representative tens-of-nanometer gold morphologies examined here are widely employed in a variety of plasmonics applications, lying within an intermediate nanoscale size range that precludes quantum confinement effects but still exhibits high (and highly tunable) surface-to-volume ratios. A rich interplay thus naturally emerges between surface versus bulk excitation and emission pathways, which can both contribute to energy flow but with different hot carrier spatial, temporal, and momentum distributions. The challenge is distinguishing these interfacial versus ballistic dynamical effects and energy-resolved population kinetics, which we achieve here utilizing simultaneous time, angle, and energy resolution.

Results and Discussion

Two-color photoemission from single nanoparticles

The experimental configuration for time- and angle-resolved scanning photoemission spectroscopy is shown in Figure 1, with two ultrafast laser pulses spaced by a variable time delay focused within vacuum to a diffraction-limited spot through a transparent, nanoparticle-coated sample. Photoemission is collected as a function of scanning sample position and photoelectron velocity is determined by mapping onto a spatially-resolved detector. Further details on the experimental technique are provided in Methods. To clarify the effects of shape, size, and

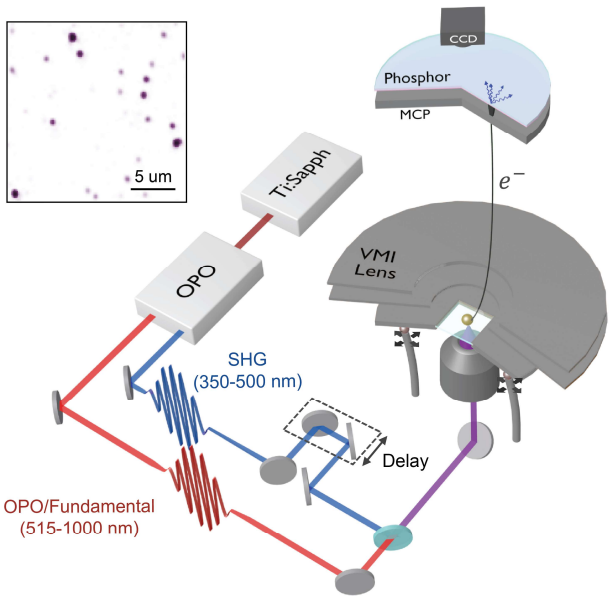

Figure 1. Time-resolved scanning photoemission spectroscopy. Femtosecond dynamics in single nanoparticles measured via pump-probe excitation and velocity-resolved photoelectron mapping. Inset: Spatially-resolved scanning photoemission map (linear scale) of gold nanorods, with a range of photoemissivities due to different nanorod resonances and orientations with respect to the linearly-polarized light excitation axis.

crystallinity on hot electron dynamics, two distinctly different nanoparticle geometries are investigated: monocrystalline gold nanorods and polycrystalline gold/silica nanoshells (Figure 2a). Small gold nanorods coated in cetyltrimethylammonium bromide (CTAB) stabilizing ligands with 10(1) nm diameter and 41(4) nm total tip-to-tip length (standard deviations in parenthesis) exhibit an average longitudinal dipolar surface plasmon resonance (SPR) around 710 nm when supported on an indium tin oxide (ITO) substrate. The ITO substrate provides charge neutralization upon photoemission and good visible light transmission in the experimental configuration. For our much larger gold/silica nanoshells with lipoic acid stabilizing ligands, 160(7) nm overall diameter, and 120(4) nm silica core diameter, we observe an average dipolar SPR on ITO around 675 nm.[33] Although the potential role of ligands or other surface effects will be considered where relevant, no effects on the photoelectron angle/energy distributions or lifetimes are observed. Recent studies of dielectric-coated nanorods have found that CTAB-coated nanorods behave as "bare" nanoparticles (i.e., the zero-thickness dielectric limit).[41]

To overcome gold nanoparticle work functions (> 4 eV) while taking advantage of plasmonic enhancements for high signal contrast between nanoparticles and the ITO substrate, we perform two-color pump-probe measurements. Both nanorod and nanoshell samples are resonantly excited with a 1.77 eV (700 nm) pump photon, after which a non-resonant 3.1 eV probe photon ejects the hot electrons into vacuum. The $1 + 1'$ 2PPE process order is verified by the pump-probe signal intensity dependence (Figures 2b and 2c), holding one beam intensity

fixed while varying the other. The linear intensity dependencies observed here and the lack of tip/surface-like emission discussed below for the nanorods/nanoshells verify the perturbative excitation regime. To leading order in each process, the overall photoemission rate is

$$\Gamma_{\mathrm{PE}} = \sigma_{\mathrm{pp}}^{(1+1')} I_{\mathrm{pump}} I_{\mathrm{probe}} + \sigma_{\mathrm{pump}}^{(3)} I_{\mathrm{pump}}^{3} + \sigma_{\mathrm{probe}}^{(2)} I_{\mathrm{probe}}^{2} + \Gamma_{\mathrm{ITO}}, \qquad (1)$$

in which the first term is the pump-probe signal of interest, while the remaining terms are weaker contributions from single-color pump 3PPE, probe 2PPE, and corresponding (weaker still) contributions from the ITO substrate. The pump-probe photoemission cross-section, $\sigma_{\mathrm{pp}}^{(1+1')}$, and the single-color photoemission cross-sections, $\sigma_{\mathrm{pump}}^{(3)}$ and $\sigma_{\mathrm{probe}}^{(2)}$, are determined experimentally for each nanoparticle under pump-probe, pump-only, and probe-only exposures. The pump-

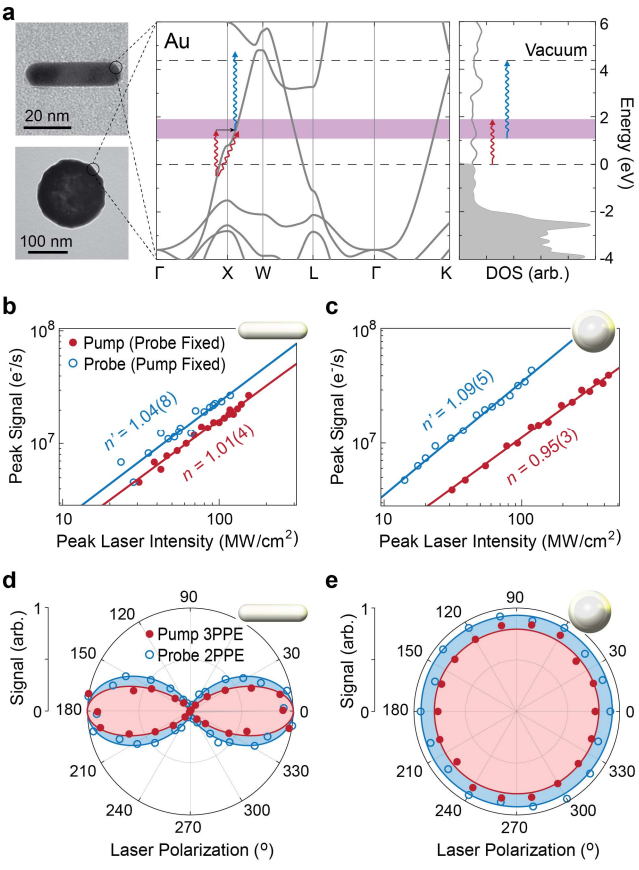

Figure 2. Two-color resonant + non-resonant pump-probe photoemission from gold nanorods and nanoshells. (**a**) Transmission electron micrographs of a representative gold nanorod and gold nanoshell, shown alongside the electronic structure and density of states of gold (Supporting Information). For visible pump photon energies, phonon/defect-mediated and/or field-gradient-assisted intraband transitions are the dominant photoexcitation mechanisms leading to intermediate state (hot carrier) population. The purple zone indicates the overlap between the excitation and probing ranges for a 1.77 eV pump, 3.1 eV probe, and ~4.15 eV nanoparticle work functions. (**b**) Nanorod and (**c**) nanoshell laser intensity-dependent pump-probe photoemission signal, with one beam held fixed at an intermediate intensity while varying the other. Solid lines are power-law fits, verifying the $n + n' = 1 + 1'$ two-color 2PPE process in each case. (**d**) Nanorod and (**e**) nanoshell polarization-dependent single-color nonlinear photoemission signal, illustrating the strong nanorod longitudinal coupling for both pump and probe beams, compared with the polarization-insensitive nanoshell excitation. Solid lines are from finite element calculations (Methods), with the simulated plasmonic field enhancements, $|E/E_0|^{2n}$ (for single-color n-photon photoemission), integrated over the respective gold volumes.

probe contribution to the total signal is then optimized under I_{pump} conditions for which $\sigma^{(2)}_{\mathrm{probe}} I^2_{\mathrm{probe}} \approx \sigma^{(3)}_{\mathrm{pump}} I^3_{\mathrm{pump}}$.

For the nanorods, the various single- and multi-photon cross-sections depend not only on the excitation frequencies, but also strongly on the linear polarization angles of both pump and probe beams, as demonstrated in Figure 2d for pump 3PPE ($\cos^6\theta$) and probe 2PPE ($\sim \cos^3\theta$; with the non-resonant interaction deviating from simple $\cos^{2n}\theta$ dependence). This strong polarization dependence is due to the larger polarizability and stronger electric field enhancements for the resonant pump beam as well as for the non-resonant probe beam when the incident field is aligned along the longitudinal nanorod axis (Fig. S8), which is utilized to determine the angle of each nanorod investigated. By contrast, the nanoshell photoemission signal displays no polarization dependence (Figure 2e), as expected for the azimuthal symmetry of the supported spherical nanoshell in the absence of surface defect hot spots.[33, 34] The single-particle resolution accompanied by insights from polarization dependent photoemission rates is invaluable for identifying/excluding clusters or particles with defects. It should also be noted that, despite the several hundred-fold larger area excited on the ITO substrate compared with the geometrical nanorod cross sections, the nanorod pump-probe signal is approximately five-fold stronger than the ITO contribution. This is attributed to the plasmon-enhanced pump and enhanced off-resonant probe absorption cross-sections.

Nanoscale geometry-insensitive carrier dynamics

Nanoplasmonic photoexcitation and transfer/emission can take place directly at the surface or ballistically from within the bulk.[35, 42-45] Direct surface excitations into hybridized metal-admolecular energy states,[42, 43, 46-49] across metal-semiconductor Schottky barriers,[5, 50] or over metal-vacuum barriers[51-53] occur predominantly within plasmonic surface hot spot regions and effectively bypass hot carrier dynamics within the metal. Time-resolved studies of such systems may thus reflect the ultrafast interfacial state dynamics.[46, 50] For gold nanorods and nanoshells, however, it has been shown that resonant photoexcitation in the multiphoton regime occurs predominantly in field-enhanced regions within the volume of the metal nanoparticles.[34, 35] This has not yet been clarified in the single-photon regime, in which bulk-like excitation at visible light frequencies involve intraband transitions with momentum conserved either by

phonon/defect scattering or field-gradient-assisted damping (Figure 2a).The latter is due to large momentum components of rapidly spatially-varying plasmonic fields, which are known to occur in surface field regions of plasmonic particles or dimers[54] but have also recently been shown to significantly enhance volume intraband photoluminescence in gold nanorods.[55] With the three-fold smaller nanorod diameters and even more dramatic internal field variations in the present studies (Figure S8), significant volume excitation density from internal field-gradient-assisted damping may be expected. Other momentum-conserving excitation pathways, including intraband excitation from electron-electron scattering[56] and interband absorption from 5d-band initial states (~2 eV below the Fermi level), yield lower-energy carriers are not probed herein. In particular, any emission pathway involving interband excitation requires an additional photon compared with intraband absorption from the Fermi level for the photon energies utilized herein.

For the pathways that can contribute to final electron states above the vacuum level, transport of the photoexcited electrons to the interface can be treated as a three-step ballistic process[57]: (i) photoexcitation within the metal, (ii) transport to an interface with quasi-elastic (e.g., electron-phonon) and inelastic (electron-electron) scattering along the way, and (iii) possible photoinjection into the surrounding medium given sufficient surface-normal momentum. While phenomenological, this semi-classical model captures the same essential features of the dynamics as the more rigorous one-step quantum theory of excitation from Bloch states into damped, inverse low-energy electron diffraction final states.[58, 59]

Energy-integrated response functions of the ballistic hot electron dynamics are determined via cross-correlation measurements (Figures 3a and 3b). The lower end of the accessible $E - E_{\mathrm{F}} \approx 1.1$–$1.8$ eV intermediate state excitation energy range is constrained by the difference between the probe photon energy (3.1 eV) and the measured gold nanoparticle work function (~4.15 eV; see below), while the upper end is constrained by the pump photon energy (1.77 eV). Hot electron dynamics are extracted from pump-probe time delay traces via the rate equation for the intermediate ($|m\rangle$) state population,[25]

$$\dot{N}_m(t) = \frac{\sigma_{im} I_{\mathrm{pump}}(t)}{\hbar\omega_{\mathrm{pump}}} - \frac{1}{\tau_{ee}(E_m)}\, N_m(t), \qquad (2)$$

where σ_{im} is the absorption cross-section for the initial state ($|i\rangle$) to $|m\rangle$ transition and $\tau_{ee}(E_m)$ is the hot electron lifetime (T_1 population decay time) at E_m. This simple limiting form of the three-level optical Bloch equations[21, 60] is well established in the case of rapid dephasing of any

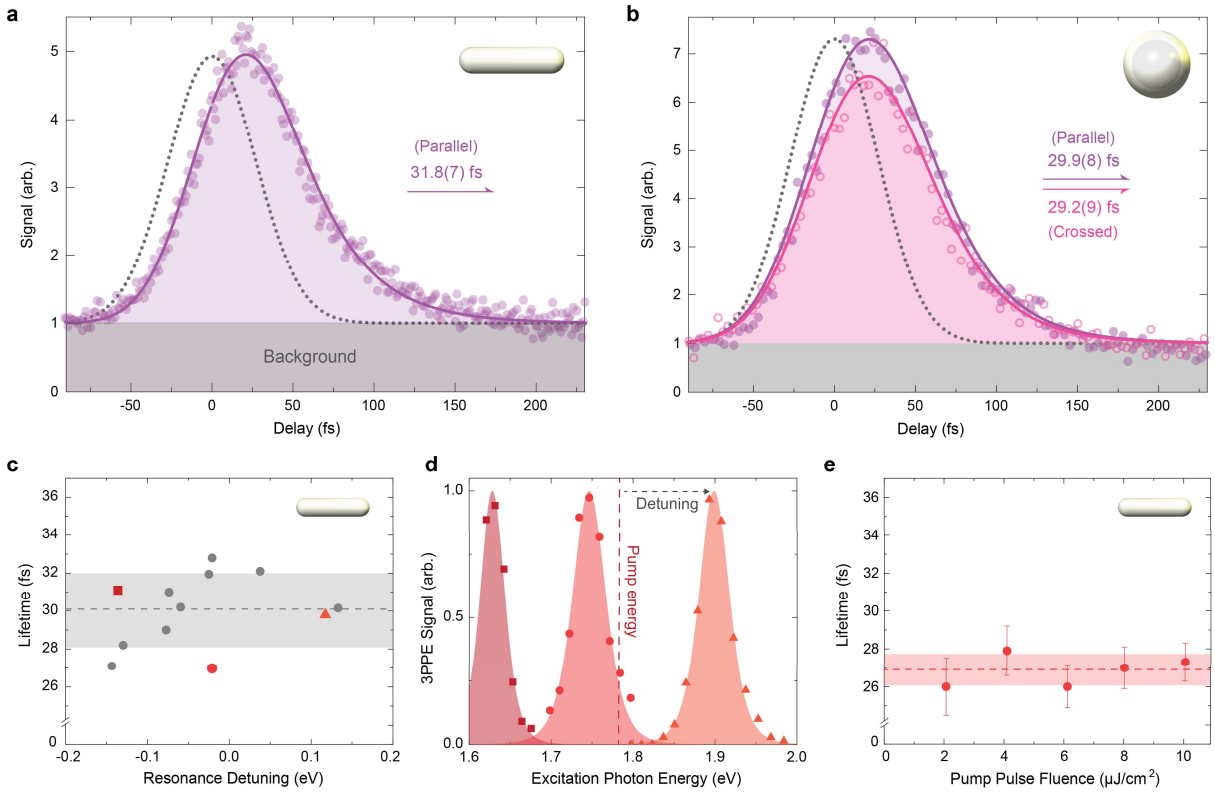

Figure 3. Energy-averaged femtosecond dynamics in single nanoparticles. (**a**) Nanorod time delay scan fit to the instrument response function (dotted line) convolved with a forward exponential hot electron response. The instrument response function is the pump-probe cross-correlation measured on the ITO substrate with an unresolvable fast (< 10 fs) response time. Due to the strong longitudinal nanorod coupling of both pump and probe beams, data is collected with parallel-polarized pump and probe beams along this axis. (**b**) Nanoshell time delay scans and fits with both parallel- and cross-polarized pump and probe beams. (**c**) Summary of lifetimes with respect to longitudinal dipolar SPR detuning from the pump photon energy (1.77 eV) for 12 nanorods, with a mean value of 30.1 fs and a standard deviation of 1.9 fs. (**d**) Single-color 3PPE spectra are shown for three representative nanorods, along with third-power Lorentzian fits, with the colors and point shapes consistent with the corresponding nanorods in panel c. The dashed line indicates the pump photon energy used in pump-probe studies. (**e**) Lifetimes are independent of incident power, as measured for a representative nanorod (same as red dot in panel c) across the relevant pump pulse fluence range utilized in these studies.

coherences relative to population times, as expected for continuum transitions.[22, 25, 61] The solution of eq 2 is determined via bilateral Laplace transform, yielding the convolution $N_m(t) \propto \int_{-\infty}^{\infty} I_{\text{pump}}(t-\tau)\, R_e(\tau) d\tau$, in which $R_e(\tau)$ is the hot electron impulse response, given by $\Theta(\tau) e^{-\tau/\tau_{ee}(E_m)}$, where Θ is the Heaviside function. The photoemission rate as a function of time delay, $\dot{N}_f(t)$, is then proportional to the cross-correlation of $N_m(t)$ with $I_{\text{probe}}(t)$. It should be noted that while reverse decay contributions from the probe-first $(1' + 1)$ excitation pathway can also occur, these contributions are negligible due to the much shorter average lifetime in this higher hot carrier energy range.

Cross-correlation fits to the solution of eq 2 are shown in Figures 3a and 3b, yielding energy-averaged lifetimes of 31.8(7) fs for the nanorods and 29.9(8) fs for the nanoshells. Broadly speaking, this agreement suggests that the nanoparticle geometry in the tens-of-nanometer size range has little effect on the hot electron decay, which is instead primarily influenced by the nanoparticle material itself. Closer examination reveals several more specific implications: First, due to the large difference in surface-to-volume ratios for the nanorods ($S/V = 0.5$ nm^{-1}) and nanoshells ($S/V = 0.1$ nm^{-1}), it is evident that the surface must play a relatively minor role in the hot electron decay, at least in the absence of surrounding media with interfacial states/barriers in the relevant energy range. This is consistent with previous studies of hot carrier thermalization times in gold and silver nanosphere ensembles, with times decreasing appreciably from the metal film limit only for very small (< 10 nm) diameters.[62] Second, the similar lifetimes provide evidence that charge transfer to the ITO substrate is small in both systems, as this would be expected to accelerate the decay measured for the nanorods relative to the nanoshells. In the nanorods, the hot carriers are all excited within an inelastic mean free path of the substrate interface, whereas most of the hot carrier density that is probed/emitted occurs at the sides of the nanoshell, well away from the small ratio of the surface area in contact with the substrate.[34] Furthermore, transfer over a small contact potential or ligand barrier would contribute to an energy dependence depends on the mean time it takes to reach the relevant interface and thus the hot carrier group velocity ($\hbar^{-1}\,\partial E/\partial k$, with E referenced to the conduction band minimum), which changes very little in the energy range of interest. Instead, we observe the strong dependence on excitation energy consistent with hot-cold electron-electron scattering (see below). Finally, the monocrystallinity of the nanorods[63-65] versus polycrystallinity of the nanoshells[66, 67] evidently has little effect on the hot electron decay times, which can be rationalized in terms of the quasi-elastic nature of the electron-phonon/defect scattering mediated by the grain boundaries.

A handful of nanorods with different SPRs are examined at constant pump photon energy (Figure 3c,d), showing little evidence of detuning effects on the hot electron decay. In each case, the pump power is adjusted for consistent pump-probe count rates and therefore excited carrier densities. However, carrier density is also found to have no observable effect on the average lifetime, as measured on a single representative nanorod over a range of pump fluences (Figure 3e) corresponding to calculated peak electron temperatures between 800–1700 K (see two-

temperature modeling described in Supporting Information). These findings are in good agreement with the full kinetic theory described below, which indicates a mere ~10% increase in the average lifetime from the zero temperature limit up to 1500 K peak temperature (Figure S6). This insensitivity to fluence precludes any significant decay contributions from hot-hot carrier-carrier scattering/recombination, the rates of which would depend on fluence via excited carrier density.

For nanorods, parallel pump and probe polarizations aligned along the longitudinal axis are necessary for measurable pump-probe signal due to the strongly enhanced light-matter interactions (Figure 2d). By contrast, both parallel- and cross-polarized beam configurations can be utilized for the azimuthally symmetric gold nanoshells. We find that the total pump-probe signal in the cross-polarized configuration is reduced by only 14%, with a negligible effect on the energy-averaged hot electron lifetime (Figure 3b). While this would be expected for bulk and thin films, a unique feature of nanoplasmonic systems is the dramatically spatially-varying field profiles that depend strongly on incident optical parameters, including polarization and frequency. Such a minor change in pump-probe signal for cross-polarized nanoshell excitation is thus noteworthy, providing information on the electric field profiles and bulk- versus surface-mediated excitation pathways. Specifically, simulations reveal that this strong cross-polarized pump-probe signal could only occur for bulk-like probe photon absorption, as the internal field is nearly isotropic for the probe excitation (Figure S8). The probe surface field, by contrast, is strongest along the polarization axis and therefore well separated by distances greater than the ~40 nm inelastic mean free path from the pump excitation region, which lies along the pump polarization axis for either surface or bulk excitations[34] (Figure S8). This strongly suggests that only bulk-like ballistic dynamics are probed within the nanoshells, as unambiguously confirmed below for nanorods via full velocity-resolved pump-probe studies.

Velocity-resolved ballistic dynamics

A two-dimensional (2D) projected velocity distribution for single nanorod excitation at the peak pump-probe time delay is shown in Figure 4a, along with a central slice of the corresponding reconstructed 3D distribution. The 3D reconstruction is performed via inverse Abel transform using the Gaussian basis set expansion (BASEX) method,[68] which relies on the approximate cylindrical symmetry in the photoemission distribution with respect to the

longitudinal nanorod axis to compensate for information loss in the experimental 2D projection (effects of deviations from perfect cylindrical symmetry are discussed in Methods). The angle-integrated kinetic energy spectrum is then determined (Figure 4c) from the reconstructed 3D distribution, with the background (i.e., non-pump-probe) contribution isolated at large time delays. It is noted that the measured spectrum is consistent with an approximate uniform excitation of nascent carriers, as described in further detail below in comparison with Boltzmann theory calculations.

Even without 3D reconstruction, the 2D photoelectron velocity map offers considerable insight into nanorod hot carrier excitation and momentum distributions. Despite the longitudinal laser polarization, volume-mediated photoexcitation yields predominantly *transverse* ballistic hot electron escape predominantly from the nearby side walls, which have a three-fold larger surface area than the tips and lie within the few-nanometer inelastic mean free path of the final-state

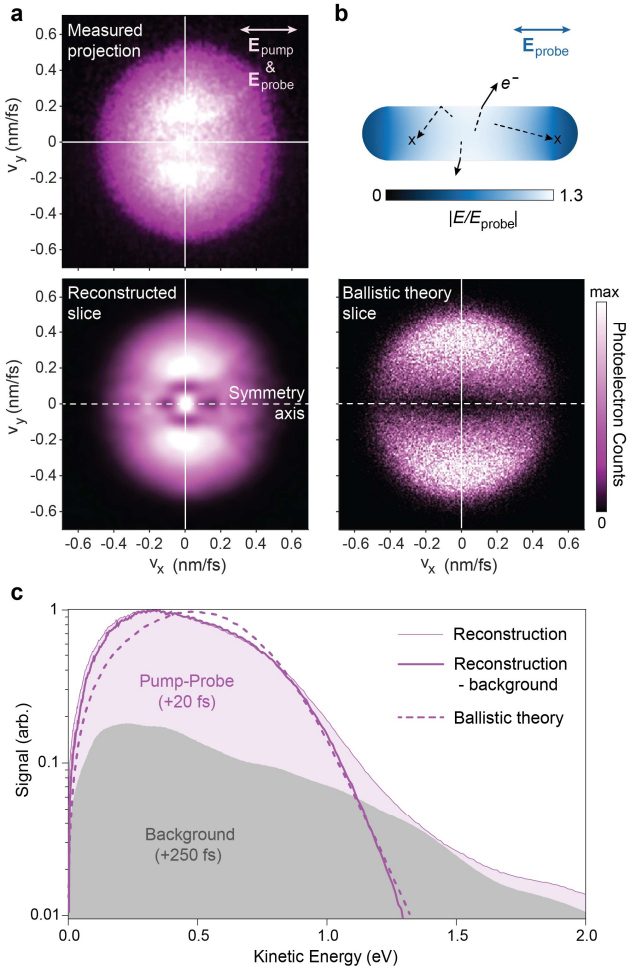

Figure 4. Pump-probe photoelectron velocity and kinetic energy distributions for a single gold nanorod. (**a**) Measured projected velocity map and central xy slice of the inverse-Abel reconstructed 3D distribution, with the axis of approximate cylindrical symmetry indicated. The zero-velocity peak is from ITO background counts. (**b**) Volume xy slice of simulated internal field enhancement distribution under probe excitation, illustrating the Monte Carlo ballistic hot electron trajectory modeling, leading to the calculated velocity distribution slice shown beneath it. In both the measured and calculated distributions, the photoemission is predominantly *transverse* with respect to the nanorod longitudinal axis under longitudinal pump and probe polarizations. (**c**) Photoelectron kinetic energy distribution determined via angular integration of the reconstructed 3D distribution, along with the background-subtracted reconstructed distribution and the (background-free) ballistic theory result.

electrons excited near the center of the nanorod.[35] This leads to an orthogonal photoemission velocity distribution with respect to the longitudinal dipolar plasmon axis. In a recent study of gold nanorods, similar orthogonal emission behavior clarified the bulk-like nature of single-color multiphoton photoemission, which transitioned to a surface regime only with sufficient red detuning.[35] This was demonstrated for nanorod resonances across the 2–4PPE regimes, with a greater tendency toward bulk-like excitation for lower-order processes due to a stronger dependence on the integrated volume field rather than the peak surface field. Bulk-like intraband excitation are therefore expected to be dominant for bare nanorods—as well as nanoshells[34] and various other gold nanoparticle geometries—in the resonant one-photon absorption limit.

While bulk-like excitation and emission has been observed for single-color multiphoton excitation, it has not yet been observed for an incoherent pump-probe excitation pathway (via population of a real intermediate hot carrier state), which offers different perspective and time resolution. The observed orthogonal photoemission for the two-color resonant + non-resonant pump-probe excitation (Figure 4a) is consistent with the resonant pump absorption occurring predominantly throughout the field-enhanced central nanorod region (Figure S8), although this may also occur due to rapid hot electron diffusion throughout the nanorod following surface-like excitation at the nanorod tip hot spots. In either case, the orthogonal photoelectron velocity distribution reveals that the non-resonant probe photon absorption occurs throughout the volume of the nanorod. As a result, the probed dynamics are necessarily ballistic rather than interfacial in nature. Indeed, considering the similar nanorod and nanoshell lifetimes, the surface appears to play little role beyond defining the boundary conditions for the plasmon modes and corresponding field distributions, even in nanoparticles with dimensions as small as 10 nm.

By way of theoretical comparison, the velocity-resolved photoemission distribution is calculated for a gold nanorod (Figure 4b) using Monte Carlo sampling of ballistic final state electron trajectories, accounting for angle- and energy-dependent transmission at the surface potential barrier (further details in Methods). We approximate rapid superdiffusive transport of the pump-excited hot electrons throughout the volume of the nanorod (elastic electron-phonon mean free path ~30 nm; energy-averaged inelastic mean free path of ~40 nm measured above in Figure 3a for a gold Fermi velocity of 1.4 nm/fs in gold). The final state photoexcitation density is then proportional to the spatial distribution of I_{probe} within the nanorod (Figure 4b). The calculated 3D velocity slice shown in Figure 4b exhibits similar transverse photoemission

behavior to that observed experimentally, with the corresponding kinetic energy distribution in Figure 4c calculated using the internal hot electron energy distribution obtained via kinetic Boltzmann theory (see below and Supporting Information) for a superheated electron gas (~1500 K; Figure S3). Fermi edge fits to measured kinetic spectra from four nanorods (all studied below with full energy- and time resolution) yield a value of $E_F = 4.15$ eV, leading to good agreement between measured and calculated spectra in Fig. 4. While some disagreement between the calculated and measured spectra is evident, the experimental distribution verifies the bulk-like model of a nearly constant excitation matrix element and approximately uniform promotion of Fermi sea electrons (the so-called random-k approximation[57, 69]), notably lacking any evidence of discrete energy levels that may occur in excitations mediated by interfacial states.

Single-particle energy-resolved femtosecond lifetimes

By combining both time and velocity resolution, the full energy-resolved femtosecond dynamics of hot electrons are measured in single resonantly-excited gold nanorods (Figure 5a). As summarized in Figure 5c, the lifetimes depend approximately inverse quadratically on the excitation energy (hot carrier energy), $E - E_F$. While this appears characteristic of Fermi liquid behavior (see Supporting Information) observed in nearly-free-electron systems such as aluminum and noble metals,[23] we offer a more rigorous analysis of the hot electron dynamics that also accounts for the femtosecond pulsed excitation, plasmon-enhanced superheating of the electron gas, electron-phonon coupling, and cascading/in-filling from higher energy levels. The temporal evolution of the hot electron distribution function, $f(E,t)$, is determined via the kinetic Boltzmann equation,

$$\frac{df(E,t)}{dt} = H(E,t) + \frac{df(E,t)}{dt}\Big|_{e-e} + \frac{df(E,t)}{dt}\Big|_{e-ph}, \quad (3)$$

in which $H(E,t)$ is the time-dependent optical excitation of hot electrons, which proceed to relax via electron-electron and electron-phonon scattering (second and third terms, respectively). The electron-electron coupling is described by a screened Coulomb potential using the approximated Thomas-Fermi expression with a phenomenologically reduced screening wavevector βk_{TF}, such that $\beta = 1$ yields Thomas-Fermi screening while $\beta < 1$ corresponds to reduced screening and stronger electron-electron interactions.[62] The electron-phonon coupling is modeled via

interaction potential with an effective deformation potential constant. Further details on the Boltzmann theory implementation, including collision integrals, are described in previous work,[70] in the Methods, and in the Supporting Information. Absorbed energy densities consistent with experiments are utilized in the calculations, corresponding to a peak electron temperature of 1500 K as determined via two-temperature modeling (Supporting Information). Considering the rapid superdiffusive/ballistic spread of pump-excited hot electrons throughout the relevant probing region (Fig. 4b), spatial degrees of freedom are neglected in eq 3 for the hot carrier intermediate state. However, as described above, the final-state electron spatial and momentum distributions are treated explicitly via Monte Carlo modeling. In larger nanoparticle systems (> 30 nm), an explicit treatment of intermediate-state (hot carrier) transport effects becomes necessary.[38]

The Boltzmann theory results are shown in Figure 5b and lifetimes are summarized in Figure 5c, with a value of $\beta = 0.9$ yielding best agreement with experiment. The power-law exponent of the energy-dependent lifetimes predicted by the kinetic Boltzmann theory is

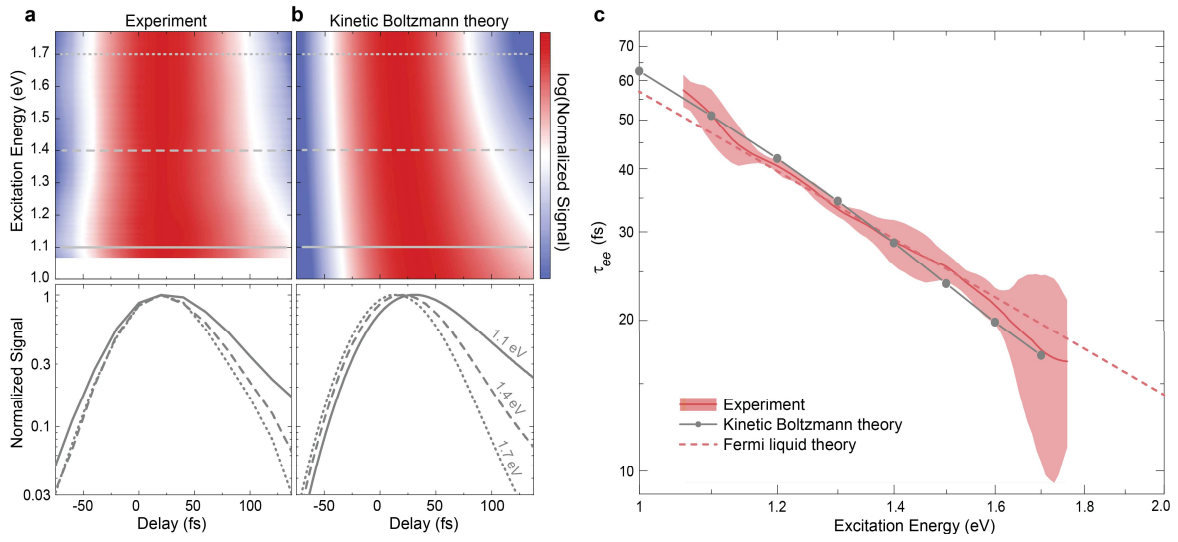

Figure 5. Energy-resolved ballistic hot electron lifetimes in single gold nanorods. (**a**) Experimental and (**b**) theoretical log-scale colormaps of the time-resolved pump-probe signal for a range of intermediate state excitation energies, $E_m = E - E_F$. The peak signal at each energy is normalized for clearer visual comparison of the dynamics. Lineouts of the cross-correlation time traces for three different excitation energies are shown in the bottom panels, with corresponding lines (and line styles) indicated in the top panels. (**c**) Summary of hot electron lifetimes for the full measurable excitation energy range. Experimental average measured for four nanorods (shaded region is the standard deviation). The oscillations are attributed to integrated white noise from the velocity maps and vary from rod to rod. Kinetic Boltzmann theory with screening parameter $\beta = 0.9$ shown for comparison, along with the best Fermi liquid theory fit ($r_s = 1.87$; Supporting Information).

approximately $m_{\mathrm{B}} = -2.4$, which is steeper than Fermi liquid theory ($m_{\mathrm{FLT}} = -2.0$) due primarily to the influence of the longer-lived hot electron tail on the lower-energy states (Supporting Information). In the zero-temperature limit (Figure S6), $m_{\mathrm{B}} \to -2.1$, still slightly elevated above the Fermi liquid theory value due to weak cascaded in-filling from higher to lower energy levels. The role of cascading is generally small for intermediate state energies greater than half the pump photon energy (> 0.9 eV here).[71] The effect of electron-phonon scattering is found to be negligible for the experimentally probed excitation energies, but quite significant for longer time scale relaxation kinetics in the < 1 eV range (Figure S4). Experimentally, a power law fit with $m_{\mathrm{exp}} = -2.3(1)$ is suggestive of the strong transient electron heating and corresponding deviations from Fermi liquid theory predicted by the full kinetic treatment, though such discrepancies remain unclear within experimental uncertainty and require further investigation. With a single-parameter fit, the Boltzmann theory also provides an extrapolation of the experimental values across the full hot electron and hole distributions (Figure S2 and Movie S1), with much longer decays in in the low energy range that deviate considerably from single-exponential behavior due to more significant contributions from cascading, electron-phonon scattering, and thermalized electrons.

The hot electron lifetimes measured in single gold nanorods (Figure 5c) lie between the ~30% smaller values measured previously for bulk gold[72] and the ~50% larger values measured for thin gold films.[23, 72, 73] This can be attributed to two competing effects that are avoided in the present study: transport and *d*-band excitations. Hot carrier transport out of the probing region leads to faster lifetimes measured in bulk metals compared with thin 10–25 nm films, where the hot carriers are constrained to a region around the escape depth.[72, 73] Transport is clearly also highly restricted in the nanoparticle limit, leading to longer hot carrier lifetimes than bulk gold values. Additionally, unlike in the preponderance of single-color femtosecond 2PPE studies of utilizing > 2 eV pump and probe photons, the plasmon-resonant pump photon energy (1.77 eV) used here lies below the ~2 eV *d*-band onset (Figure 1a) and precludes interband pump absorption, while the fluence of the probe beam is relatively weak. The lifetimes measured here are therefore unaltered by *d*-band effects—most prominently, the delayed Auger decay of *d*-band holes[23]—which we suggest leads to the faster values compared with previous thin film measurements. Most importantly, a wide variety of gold nanostructure geometries away from

spherical limit exhibit < 2 eV (> 620 nm) resonances that similarly minimize the influence of d-band absorption in typical applications.

Other effects that have been shown to influence lifetimes in the nanoconfined limit are avoided here as well. In particular, electron wavefunction spillout and d-band related screening reduction in surface atomic layers leads to enhanced electron-electron interactions that reduce hot carrier thermalization times (relative to Au films) for < 10 nm nanoparticles.[19, 62] However, the > 10 nm nanoparticle dimensions and nearly identical average lifetimes measured in nanorods and nanoshells suggest that such effects are negligible in the present studies. While quantum confinement in few-nanometer metal clusters may increase hot carrier lifetimes relative to thin metal films[24] due to a reduced density of states and therefore reduced electron-electron interactions,[74, 75] the nanoparticles studied here are well beyond this size regime.

Conclusions

Having verified the probing of internal ballistic dynamics for isolated gold nanorods and nanoshells, we find that such intermediate-nanoscale geometries offer an unadulterated view of the intrinsic electron-electron decay times in gold. This also suggests that nanoparticles can serve as an excellent platform for isolating interfacial effects (e.g., direct excitation or indirect scattering into surface-localized states) upon the introduction of various surrounding media, with particularly high surface-to-volume ratios and the ability to tailor surface- vs. bulk-localized fields. Along with dynamical insights that have become apparent in these single-particle velocity-resolved studies, the kinetic lifetimes measured here also provide the first direct experimental benchmark for energy-resolved femtosecond hot electron decay in nanoscale gold. We have shown that these lifetimes are insensitive to the nanoparticle geometry and crystallinity, and instead represent the intrinsic dynamics of the metal. These results can thus be applied to other gold structures, including extended films and bulk systems, while qualitative features of the nanoscale dynamics can be extended to other noble metals. It is our hope that such insights may be utilized to improve upon the generally low ($< 1\%$) ballistic hot carrier collection efficiencies observed to date, which represents a crucial challenge for the development of next-generation hot carrier optoelectronic and photocatalytic devices.

Methods

Sample Preparation

The quality and dimensional statistics of commercially-purchased nanorod (Nanopartz Inc.) and nanoshell (nanoComposix) samples are verified via transmission electron microscopy (FEI Tecnai T12 SpiritBT, 100 kV, LaB_6 cathode) after drop-casting 15 μL of the aqueous dispersions onto a carbon-coated TEM grid for 5 minutes, removing the excess solution, and drying in air. Samples are then prepared for photoemission studies by spin-coating 50 μL aliquots at 1500 rpm onto ITO-coated (10 nm) borosilicate coverslips ($<$ 1 nm RMS surface roughness). UV-ozone cleaning of the substrates prior to deposition ensures good wetting. Nanoparticle solutions are diluted prior to deposition to ensure appropriately dense surface coverages ($\sim$5 nanoparticles per 10×10 μm^2 area) with average particle separations much greater than the diffraction-limited beam spot. Samples are prepared under ambient conditions and loaded into vacuum immediately upon preparation. Nanoparticles are "cleaned" under vacuum prior to all studies via brief ($\sim$1 s) exposure to high-intensity ($\sim$1 GW·cm^{-2}) 400 nm light in an area scan, which has been shown to reversibly remove air contaminants and eliminate post-emission scattering that obscures the final velocity distribution.[33, 76]

Scanning Photoemission Imaging Microscopy

Our scanning photoemission imaging microscopy (SPIM) technique combines ultrafast pump-probe excitation, scanning photoemission microscopy, and velocity map imaging photoemission spectroscopy, enabling single-nanoparticle time-, angle-, and energy-resolved photoemission studies. The second harmonic of a Ti:sapphire oscillator (KMLabs Swift, 75 MHz, $\sim$50 fs pulses, 700–1000 nm tuning) pumps an optical parametric oscillator, with the tunable signal beam output (515–775 nm) serving in these experiments as the plasmon-coupled pump beam. The remainder of the second harmonic (400 nm, 3.1 eV) serves as the probe beam, with the relative delay time scanned with a motorized delay stage in the probe beam path, as illustrated in Figure 1. The pump and probe pulse durations are both approximately 50 fs, as determined by frequency-resolved optical gating measurements at the laser output and by photoemission cross- and auto-correlation measurements directly at the sample position (on the ITO substrate). The high repetition rate offers high signal-to-noise while precluding space-charge repulsion (only one electron is emitted every $\sim 10^6$ pulses at most) and, more importantly, event

overlap on the spatially-resolved detector. While highly tunable, the pump beam is maintained at 700 nm for the present pump-probe studies for (i) optimal plasmon-resonant coupling for both nanorods and nanoshells, and (ii) optimized dispersion compensation and pulse duration. The present measurements are not interferometrically stabilized and are thus phase-averaged. Group velocity dispersion is optimized to minimize pulse durations via dual-prism compensators in both pump and probe beam paths, with the single-color photoemission signal monitored as a function of prism pair separation and insertion into the beam path.

The two beams are focused down to overlapping diffraction-limited spots on an xy scanning sample stage using a reflective 0.65 NA microscope objective, all under high vacuum conditions (2×10^{-7} Torr), with the pump-probe photoemission collected as a function of both sample position (Figure 1 inset) and time delay. Dozens of nanoparticles can be interrogated simultaneously (within a series of scans) as a function of different incident laser parameters (intensity, frequency, and polarization) via large-area scans. Alternatively, single nanoparticles can be studied over the course of hours with little drift relative to the diffraction-limited laser spot (or for days with minor positional corrections). Larger (millimeter-scale) xy positioning and z focusing is achieved with piezoelectric motors.

Photoelectrons emitted from the sample are linearly mapped onto a phosphor-microchannel plate detector via the electrostatic lens illustrated schematically in Figure 1, which consists of three copper electrodes: (i) The sample stage (repeller electrode) biased at -4500 V, (ii) an "extractor" plate biased at -3700 V, and (iii) a final grounded electrode plate. This velocity map imaging lens configuration serves to linearly map photoelectrons from initial velocity (v_x, v_y) onto detector position (d_x, d_y), integrating over initial v_z with negligible distortion (given the much larger 4.5 keV accelerated photoelectron energies compared with < 1 eV initial energies) and little sensitivity to initial position.[77] The repeller bias is adjusted to optimize use of a 75 mm microchannel plate detector area while minimizing distortion due to electrode proximity for the outermost electron trajectories. The extractor plate bias is then optimized via ion trajectory simulations (*SIMION 8.0*) to achieve the initial-position-insensitive velocity-mapping condition.[77] The system is calibrated via laser frequency-dependent photoemission studies and Fermi edge fits for thin gold film, as described along with further details and characterization of the system in previous work.[76]

Finite Element Simulations

Finite element simulations are performed using the RF module in *COMSOL Multiphysics 6.0* using plane electromagnetic waves normally incident on ITO/glass-supported gold nanoparticles. Average nanorod and nanoshell ensemble dimensions are utilized to model the nanoparticles. Measured values from Johnson and Christy[78] are used for the gold dielectric function, while the ITO dielectric function was determined via ellipsometry. A perfectly-matched layer is utilized for domain truncation and due diligence is performed for convergence with respect to mesh, domain, and PML size. Total photoemission values are approximated by integrating the volume field enhancement raised to the $2n$ power for nPPE (thus approximating a position-independent escape coefficient). This approximation is suitable for estimating simple polarization-dependent behaviors (Figures 2d and 2e). For ballistic photoemission calculations (see below), the simulated volume field enhancement data is exported on a fine uniform mesh. Simulated surface and volume fields for both nanorod and nanoshell geometries are shown in the Supporting Information, Figure S8.

Inverse Abel Transform

Approximate 3D photoelectron velocity distributions are reconstructed from the measured 2D distributions via inverse Abel transform (where the projection in v_z constitutes the forward Abel transform). This is implemented efficiently via matrix algebra in *MATLAB* using the basis set expansion (BASEX) method of Dribinski *et al.*[68] with nearly-Gaussian basis functions. A standard deviation of $\sigma = 1$ px and regularization parameter of 10 are utilized.

The information lost in the 3D → 2D projection can be recovered if an axis of cylindrical symmetry exists orthogonal to the projection direction (i.e., within the xy plane here), thereby permitting a unique reconstruction. The validity of such an approximation is expected to be perfect for unsupported cylindrical nanorods, though could be called into question for the nanorod faceting and ITO substrate. However, the typical octagonal nanorod side faceting[65] and nominal $\cos(\theta)$ photoelectron emission distribution with respect to the local surface normal[76] yields a quasi-continuous azimuthal distribution about the nanorod longitudinal axis. Furthermore, several points can be made on the symmetry-breaking effects of the ITO substrate: (i) The internal probe field, corresponding volume hot carrier excitation density, and emission distribution remain reasonably symmetric (25% top/bottom field intensity asymmetry), including

further blurring out due to the internal ballistic dynamics. (ii) For the downward-moving photoelectron trajectories that aren't immediately beneath the nanorod (i.e., those that escape into free space), the projected velocity distribution would not be altered by angle/energy-independent specular reflection or collection by the ITO. Clearly, even basic considerations of the quantum reflection probability at a step-down barrier, $|R|^2 = |(k_\perp - k'_\perp)/(k_\perp + k'_\perp)|^2$, can be expected to distort the velocity distribution of the substrate-reflected photoelectrons and lead to deviations from perfect cylindrical symmetry. While more careful accounting of such effects may be valuable in future studies, the good agreement between the reconstructed experimental and calculated photoelectron distributions (Figure 4) suggests that these deviations are small.

Ballistic Dynamics Simulations

Briefly, for pump-probe 2PPE, it is approximated that the pump-excited hot electrons (traveling at $\gtrsim$ 1.4 nm/fs) are uniformly distributed within the nanorod when probe absorption occurs. Thus, only the internal probe field intensity distribution need be accounted for. A Monte Carlo method involving randomly-sampled trajectories for final-state electrons is then employed, taking into consideration (i) energy-dependent inelastic mean-free paths within the nanorod (extrapolated from measured lifetimes), (ii) angle- and energy-dependent quantum transmission coefficients at the metal-vacuum interface (depending on the surface-normal momentum), and (iii) "refraction" of escaped photoelectrons due to surface-normal momentum loss and parallel momentum conservation at the interfacial potential barrier. We assume a smoothed surface potential barrier here such that electrons are perfectly transmitted (reflected) if their kinetic energy corresponding to surface-normal momentum is greater than (less than) the surface potential barrier.[44] The geometry of the nanorod and the probe-intensity-weighted spatial excitation distribution (determined from finite element simulations) are fully accounted for in these calculations, which can be extended to arbitrary 3D geometries. Further details on this Monte Carlo hot electron emission modeling and context with respect to other methods are described elsewhere.[35]

Boltzmann Theory

The relaxation dynamics is modeled using the quasiparticle approach of the Fermi-liquid theory and describing the conduction-electron system by a one-particle distribution function $f(E,t)$. Its time evolution is given by the Boltzmann equation (eq 3).[12, 18, 62, 70, 79] The initial out

of equilibrium excitation by intraband absorption of a femtosecond pump pulse of frequency ω_{pump} (first term of eq 3) leads to the creation of a spatially homogeneous nonthermal distribution where conduction electrons with an initial state energy, E_i, between $E_{\mathrm{F}} - \hbar\omega_{\mathrm{pump}}$ and E_{F} are excited above the Fermi energy to an intermediate state energy, E_m, between E_{F} and $E_{\mathrm{F}} + \hbar\omega_{\mathrm{pump}}$.

Modification of Δf induced by electron-electron scattering (second term in eq 3) is described by a screened Coulomb potential, with an $|\epsilon|^{-2}$ screening factor depending on interband and Drude-like electron dielectric functions ϵ. In the limit of small wavevector and energy exchanges, $\epsilon \approx \epsilon_{\mathrm{ib}}^{0}[1 + (\beta q_{\mathrm{TF}})^2/q^2]$, where $\epsilon_{\mathrm{ib}}^{0}$ is the long-wavelength static value of the interband (i.e., from *d*-band to conduction band) electron screening contribution, q_{TF} is the Thomas-Fermi screening wavevector, β is a phenomenological screening reduction parameter, and q is the wavevector exchanged during an electron-electron collision. The screened Coulomb potential is then multiplied by electronic state occupation numbers to account for probability of transitions from occupied initial states to available final states.

The electron-phonon scattering contribution (third term in eq 3) describes electron energy loss by energy to lattice energy transfer. This is modeled starting from an interaction potential with an effective deformation potential constant and considering an isotropic band for phonon energies. Further details are provided in the Supporting Information.

Numerical computation of these three contributions leads to the full solution of the Boltzmann equation for the time evolution of $f(E,t)$. For all computations in this work, the pump pulse is set to 1.8 eV phonon energy and 50 fs duration, with an absorbed pump fluence corresponding to a peak electron temperature increase of 1200 K (Figure S3). Final Δf values are obtained after energy and time convolution of the probe pulse with 0.1 eV energy width and 50 fs time duration.

Author Information

Notes

The authors declare no competing interests.

ORCID iDs

Jacob Pettine: 0000-0003-2102-1743

Paolo Maioli: 0000-0002-4199-8810
Natalia Del Fatti: 0000-0002-8074-256X
David J. Nesbitt: 0000-0001-5365-1120

Data Sharing

All presented data and code utilized in this manuscript is available from the corresponding authors upon reasonable request.

Acknowledgements

This work was supported by the Air Force Office of Scientific Research (FA9550-15-1-0090) and the National Science Foundation Physics Frontier Center (PHY-1734006). J.P. acknowledges additional support by the Laboratory Directed Research and Development program of Los Alamos National Laboratory under project number 20210845PRD1. N.D.F acknowledges the Institut Universitaire de France (IUF).

Supporting Information

This PDF file includes:

Supporting text

Figures S1 to S8

Legend for Movie S1

SI References

Other supporting materials for this manuscript include:

Movie S1

References

(1) Cortés, E.; Besteiro, L. V.; Alabastri, A.; Baldi, A.; Tagliabue, G.; Demetriadou, A.; Narang, P. Challenges in Plasmonic Catalysis. *ACS Nano* **2020**, *14* (12), 16202-16219

(2) Lee, J.; Mubeen, S.; Ji, X. L.; Stucky, G. D.; Moskovits, M. Plasmonic Photoanodes for Solar Water Splitting with Visible Light. *Nano Lett.* **2012**, *12* (9), 5014-5019

(3) DuChene, J. S.; Tagliabue, G.; Welch, A. J.; Cheng, W. H.; Atwater, H. A. Hot Hole Collection and Photoelectrochemical CO_2 Reduction with Plasmonic Au/P-GaN Photocathodes. *Nano Lett.* **2018**, *18* (4), 2545-2550

(4) Clavero, C. Plasmon-Induced Hot-Electron Generation at Nanoparticle/Metal-Oxide Interfaces for Photovoltaic and Photocatalytic Devices. *Nat. Photonics* **2014**, *8* (2), 95-103

(5) Wu, K.; Chen, J.; McBride, J. R.; Lian, T. Efficient Hot-Electron Transfer by a Plasmon-Induced Interfacial Charge-Transfer Transition. *Science* **2015**, *349* (6248), 632-635

(6) Tagliabue, G.; Jermyn, A. S.; Sundararaman, R.; Welch, A. J.; DuChene, J. S.; Pala, R.; Davoyan, A. R.; Narang, P.; Atwater, H. A. Quantifying the Role of Surface Plasmon Excitation and Hot Carrier Transport in Plasmonic Devices. *Nat. Commun.* **2018**, *9*, 3394

(7) Goodman, A. M.; Hogan, N. J.; Gottheim, S.; Li, C.; Clare, S. E.; Halas, N. J. Understanding Resonant Light-Triggered DNA Release from Plasmonic Nanoparticles. *ACS Nano* **2017**, *11* (1), 171-179

(8) Dorodnyy, A.; Salamin, Y.; Ma, P.; Plestina, J. V.; Lassaline, N.; Mikulik, D.; Romero-Gomez, P.; Morral, A. F. I.; Leuthold, J. Plasmonic Photodetectors. *IEEE J. Sel. Top. Quantum Electron.* **2018**, *24* (6), 4600313

(9) Brongersma, M. L.; Halas, N. J.; Nordlander, P. Plasmon-Induced Hot Carrier Science and Technology. *Nat. Nanotechnol.* **2015**, *10* (1), 25-34

(10) Leenheer, A. J.; Narang, P.; Lewis, N. S.; Atwater, H. A. Solar Energy Conversion via Hot Electron Internal Photoemission in Metallic Nanostructures: Efficiency Estimates. *J. Appl. Phys.* **2014**, *115* (13), 134301

(11) Graf, M.; Jalas, D.; Weissmuller, J.; Petrov, A. Y.; Eich, M. Surface-to-Volume Ratio Drives Photoelelectron Injection from Nanoscale Gold into Electrolyte. *ACS Catalysis* **2019**, *9* (4), 3366-3374

(12) Baida, H.; Mongin, D.; Christofilos, D.; Bachelier, G.; Crut, A.; Maioli, P.; Del Fatti, N.; Vallee, F. Ultrafast Nonlinear Optical Response of a Single Gold Nanorod near Its Surface Plasmon Resonance. *Phys. Rev. Lett.* **2011**, *107* (5), 057402

(13) Hartland, G. V. Optical Studies of Dynamics in Noble Metal Nanostructures. *Chem. Rev.* **2011**, *111* (6), 3858-3887

(14) Crut, A.; Maioli, P.; Del Fatti, N.; Vallee, F. Optical Absorption and Scattering Spectroscopies of Single Nano-Objects. *Chem. Soc. Rev.* **2014**, *43* (11), 3921-3956

(15) Zavelani-Rossi, M.; Polli, D.; Kochtcheev, S.; Baudrion, A. L.; Beal, J.; Kumar, V.; Molotokaite, E.; Marangoni, M.; Longhi, S.; Cerullo, G.; et al. Transient Optical Response of a Single Gold Nanoantenna: The Role of Plasmon Detuning. *ACS Photonics* **2015**, *2* (4), 521-529

(16) Wang, J. Z.; Yu, K.; Yang, Y.; Hartland, G. V.; Sader, J. E.; Wang, G. P. Strong Vibrational Coupling in Room Temperature Plasmonic Resonators. *Nat. Commun.* **2019**, *10*, 1527

(17) Rouxel, R.; Diego, M.; Maioli, P.; Lascoux, N.; Vialla, F.; Rossella, F.; Banfi, F.; Vallee, F.; Del Fatti, N.; Crut, A. Electron and Lattice Heating Contributions to the Transient Optical Response of a Single Plasmonic Nano-Object. *J. Phys. Chem. C* **2021**, *125* (42), 23275-23286

(18) Stoll, T.; Maioli, P.; Crut, A.; Del Fatti, N.; Vallee, F. Advances in Femto-Nano-Optics: Ultrafast Nonlinearity of Metal Nanoparticles. *Eur. Phys. J. B* **2014**, *87* (11), 260-279

(19) Voisin, C.; Christofilos, D.; Del Fatti, N.; Vallee, F.; Prevel, B.; Cottancin, E.; Lerme, J.; Pellarin, M.; Broyer, M. Size-Dependent Electron-Electron Interactions in Metal Nanoparticles. *Phys. Rev. Lett.* **2000**, *85* (10), 2200-2203

(20) Pettine, J.; Nesbitt, D. J. Emerging Methods for Controlling Hot Carrier Excitation and Emission Distributions in Nanoplasmonic Systems. *J. Phys. Chem. C* **2022**, *126* (35), 14767-14780

(21) Petek, H.; Ogawa, S. Femtosecond Time-Resolved Two-Photon Photoemission Studies of Electron Dynamics in Metals. *Prog. Surf. Sci.* **1997**, *56* (4), 239-310

(22) Zhukov, V. P.; Chulkov, E. V. The Femtosecond Dynamics of Electrons in Metals. *Phys.-Usp.+* **2009**, *52* (2), 105-136

(23) Bauer, M.; Marienfeld, A.; Aeschlimann, M. Hot Electron Lifetimes in Metals Probed by Time-Resolved Two-Photon Photoemission. *Prog. Surf. Sci.* **2015**, *90* (3), 319-376

(24) Merschdorf, M.; Kennerknecht, C.; Pfeiffer, W. Collective and Single-Particle Dynamics in Time-Resolved Two-Photon Photoemission. *Phys. Rev. B* **2004**, *70* (19), 193401

(25) Bauer, M.; Aeschlimann, M. Dynamics of Excited Electrons in Metals, Thin Films and Nanostructures. *J. Electron. Spectrosc.* **2002**, *124* (2-3), 225-243

(26) Pfeiffer, W.; Kennerknecht, C.; Merschdorf, M. Electron Dynamics in Supported Metal Nanoparticles: Relaxation and Charge Transfer Studied by Time-Resolved Photoemission. *Appl. Phys. A* **2004**, *78* (7), 1011-1028

(27) Cinchetti, M.; Gloskovskii, A.; Nepjiko, S. A.; Schonhense, G.; Rochholz, H.; Kreiter, M. Photoemission Electron Microscopy as a Tool for the Investigation of Optical near Fields. *Phys. Rev. Lett.* **2005**, *95* (4), 047601

(28) Aeschlimann, M.; Bauer, M.; Bayer, D.; Brixner, T.; García de Abajo, F. J.; Pfeiffer, W.; Rohmer, M.; Spindler, C.; Steeb, F. Adaptive Subwavelength Control of Nano-Optical Fields. *Nature* **2007**, *446* (7133), 301-304

(29) Sun, Q.; Ueno, K.; Yu, H.; Kubo, A.; Matsuo, Y.; Misawa, H. Direct Imaging of the near Field and Dynamics of Surface Plasmon Resonance on Gold Nanostructures Using Photoemission Electron Microscopy. *Light Sci. Appl.* **2013**, *2*,

(30) Marsell, E.; Losquin, A.; Svard, R.; Miranda, M.; Guo, C.; Harth, A.; Lorek, E.; Mauritsson, J.; Arnold, C. L.; Xu, H. X.; et al. Nanoscale Imaging of Local Few-Femtosecond near-Field Dynamics within a Single Plasmonic Nanoantenna. *Nano Lett.* **2015**, *15* (10), 6601-6608

(31) Rohmer, M.; Bauer, M.; Leissner, T.; Schneider, C.; Fischer, A.; Niedner-Schatteburg, G.; von Issendorff, B.; Aeschlimann, M. Time-Resolved Photoelectron Nano-Spectroscopy of Individual Silver Particles: Perspectives and Limitations. *Phys. Status Solidi. B* **2010**, *247* (5), 1132-1138

(32) Gliserin, A.; Chew, S. H.; Choi, S.; Kim, K.; Hallinan, D. T.; Oh, J. W.; Kim, S.; Kim, D. E. Interferometric Time- and Energy-Resolved Photoemission Electron Microscopy for Few-Femtosecond Nanoplasmonic Dynamics. *Rev. Sci. Instrum.* **2019**, *90* (9),

(33) Pettine, J.; Grubisic, A.; Nesbitt, D. J. Polarization-Controlled Directional Multiphoton Photoemission from Hot Spots on Single Au Nanoshells. *J. Phys. Chem. C* **2018**, *122* (26), 14805-14813

(34) Pettine, J.; Marton Menendez, A.; Nesbitt, D. J. Continuous Angular Control over Anisotropic Photoemission from Isotropic Gold Nanoshells. *J. Chem. Phys.* **2020**, *153* (10), 101101

(35) Pettine, J.; Meyer, S. M.; Medeghini, F.; Murphy, C. J.; Nesbitt, D. J. Controlling the Spatial and Momentum Distributions of Plasmonic Carriers: Volume vs Surface Effects. *ACS Nano* **2021**, *15* (1), 1566-1578

(36) Lehr, M.; Foerster, B.; Schmitt, M.; Krüger, K.; Sönnichsen, C.; Schönhense, G.; Elmers, H. J. Momentum Distribution of Electrons Emitted from Resonantly Excited Individual Gold Nanorods. *Nano Lett.* **2017**, *17* (11), 6606-6612

(37) Lehr, M.; Bley, K.; Vogel, N.; Rethfeld, B.; Schönhense, G.; Elmers, H.-J. Evidence of Spatially Inhomogeneous Electron Temperature in a Resonantly Excited Array of Bow-Tie Nanoantennas. *J. Phys. Chem. C* **2019**, *123* (19), 12429-12436

(38) Jermyn, A. S.; Tagliabue, G.; Atwater, H. A.; Goddard, W. A.; Narang, P.; Sundararaman, R. Transport of Hot Carriers in Plasmonic Nanostructures. *Phys. Rev. Mater.* **2019**, *3* (7), 075201

(39) Ikhsanov, R. S.; Novitsky, A. V.; Protsenko, I. E.; Uskov, A. V. Bulk Photoemission from Plasmonic Nanoantennas of Different Shapes. *J. Phys. Chem. C* **2018**, *122* (22), 11985-11992

(40) Blandre, E.; Jalas, D.; Petrov, A. Y.; Eich, M. Limit of Efficiency of Generation of Hot Electrons in Metals and Their Injection inside a Semiconductor Using a Semiclassical Approach. *ACS Photonics* **2018**, *5* (9), 3613-3620

(41) Medeghini, F.; Pettine, J.; Meyer, S. M.; Murphy, C. J.; Nesbitt, D. J. Regulating and Directionally Controlling Electron Emission from Gold Nanorods with Silica Coatings. *Nano Lett.* **2022**, *22*, 644-651

(42) Wolf, M.; Hotzel, A.; Knoesel, E.; Velic, D. Direct and Indirect Excitation Mechanisms in Two-Photon Photoemission Spectroscopy of Cu(111) and CO/Cu(111). *Phys. Rev. B* **1999**, *59* (8), 5926-5935

(43) Petek, H. Photoexcitation of Adsorbates on Metal Surfaces: One-Step or Three-Step. *J. Chem. Phys.* **2012**, *137* (9), 091704

(44) Uskov, A. V.; Protsenko, I. E.; Ikhsanov, R. S.; Babicheva, V. E.; Zhukovsky, S. V.; Lavrinenko, A. V.; O'Reilly, E. P.; Xu, H. X. Internal Photoemission from Plasmonic Nanoparticles: Comparison between Surface and Volume Photoelectric Effects. *Nanoscale* **2014**, *6* (9), 4716-4727

(45) Aslam, U.; Rao, V. G.; Chavez, S.; Linic, S. Catalytic Conversion of Solar to Chemical Energy on Plasmonic Metal Nanostructures. *Nat. Catal.* **2018**, *1* (9), 656-665

(46) Tan, S. J.; Argondizzo, A.; Ren, J. D.; Liu, L. M.; Zhao, J.; Petek, H. Plasmonic Coupling at a Metal/Semiconductor Interface. *Nat. Photonics* **2017**, *11* (12), 806-812

(47) Boerigter, C.; Aslam, U.; Linic, S. Mechanism of Charge Transfer from Plasmonic Nanostructures to Chemically Attached Materials. *ACS Nano* **2016**, *10* (6), 6108-6115

(48) Boerigter, C.; Campana, R.; Morabito, M.; Linic, S. Evidence and Implications of Direct Charge Excitation as the Dominant Mechanism in Plasmon-Mediated Photocatalysis. *Nat. Commun.* **2016**, *7*, 10545

(49) Foerster, B.; Joplin, A.; Kaefer, K.; Celiksoy, S.; Link, S.; Sonnichsen, C. Chemical Interface Damping Depends on Electrons Reaching the Surface. *ACS Nano* **2017**, *11* (3), 2886-2893

(50) Foerster, B.; Hartelt, M.; Collins, S. S. E.; Aeschlimann, M.; Link, S.; Sonnichsen, C. Interfacial States Cause Equal Decay of Plasmons and Hot Electrons at Gold-Metal Oxide Interfaces. *Nano Lett.* **2020**, *20* (5), 3338-3343

(51) Bormann, R.; Gulde, M.; Weismann, A.; Yalunin, S. V.; Ropers, C. Tip-Enhanced Strong-Field Photoemission. *Phys. Rev. Lett.* **2010**, *105* (14), 147601

(52) Neacsu, C. C.; Berweger, S.; Olmon, R. L.; Saraf, L. V.; Ropers, C.; Raschke, M. B. Near-Field Localization in Plasmonic Superfocusing: A Nanoemitter on a Tip. *Nano Lett.* **2010**, *10* (2), 592-596

(53) Pettine, J.; Choo, P.; Medeghini, F.; Odom, T. W.; Nesbitt, D. J. Plasmonic Nanostar Photocathodes for Optically-Controlled Directional Currents. *Nat. Commun.* **2020**, *11*, 1367

(54) Khurgin, J. B.; Tsai, W. Y.; Tsai, D. P.; Sun, G. Landau Damping and Limit to Field Confinement and Enhancement in Plasmonic Dimers. *ACS Photonics* **2017**, *4* (11), 2871-2880

(55) Ostovar, B.; Cai, Y. Y.; Tauzin, L. J.; Lee, S. A.; Ahmadivand, A.; Zhang, R. M.; Nordlander, P.; Link, S. Increased Intraband Transitions in Smaller Gold Nanorods Enhance Light Emission. *ACS Nano* **2020**, *14* (11), 15757-15765

(56) Khurgin, J. B. Hot Carriers Generated by Plasmons: Where Are They Generated and Where Do They Go from There? *Faraday Discuss.* **2019**, *214*, 35-58

(57) Berglund, C. N.; Spicer, W. E. Photoemission Studies of Copper and Silver: Theory. *Phys. Rev. A* **1964**, *136* (4a), 1030-1044

(58) Feuerbacher, B.; Willis, R. F. Photoemission and Electron States at Clean Surfaces. *J. Phys. C Solid State Phys.* **1976**, *9* (2), 169-216

(59) Feibelman, P. J.; Eastman, D. E. Photoemission Spectroscopy - Correspondence between Quantum-Theory and Experimental Phenomenology. *Phys. Rev. B* **1974**, *10* (12), 4932-4947

(60) Bauer, M.; Pawlik, S.; Aeschlimann, M. Decay Dynamics of Photoexcited Alkali Chemisorbates: Real-Time Investigations in the Femtosecond Regime. *Phys. Rev. B* **1999**, *60* (7), 5016-5028

(61) Weida, M. J.; Ogawa, S.; Nagano, H.; Petek, H. Ultrafast Interferometric Pump-Probe Correlation Measurements in Systems with Broadened Bands or Continua. *J. Opt. Soc. Am. B* **2000**, *17* (8), 1443-1451

(62) Voisin, C.; Christofilos, D.; Loukakos, P. A.; Del Fatti, N.; Vallee, F.; Lerme, J.; Gaudry, M.; Cottancin, E.; Pellarin, M.; Broyer, M. Ultrafast Electron-Electron Scattering and Energy Exchanges in Noble-Metal Nanoparticles. *Phys. Rev. B* **2004**, *69* (19), 195416

(63) Murphy, C. J.; San, T. K.; Gole, A. M.; Orendorff, C. J.; Gao, J. X.; Gou, L.; Hunyadi, S. E.; Li, T. Anisotropic Metal Nanoparticles: Synthesis, Assembly, and Optical Applications. *J. Phys. Chem. B* **2005**, *109* (29), 13857-13870

(64) Katz-Boon, H.; Rossouw, C. J.; Weyland, M.; Funston, A. M.; Mulvaney, P.; Etheridge, J. Three-Dimensional Morphology and Crystallography of Gold Nanorods. *Nano Lett.* **2011**, *11* (1), 273-278

(65) Park, K.; Drummy, L. F.; Wadams, R. C.; Koerner, H.; Nepal, D.; Fabris, L.; Vaia, R. A. Growth Mechanism of Gold Nanorods. *Chem. Mater.* **2013**, *25* (4), 555-563

(66) Oldenburg, S. J.; Averitt, R. D.; Westcott, S. L.; Halas, N. J. Nanoengineering of Optical Resonances. *Chem. Phys. Lett.* **1998**, *288* (2), 243-247

(67) Brinson, B. E.; Lassiter, J. B.; Levin, C. S.; Bardhan, R.; Mirin, N.; Halas, N. J. Nanoshells Made Easy: Improving Au Layer Growth on Nanoparticle Surfaces. *Langmuir* **2008**, *24* (24), 14166-14171

(68) Dribinski, V.; Ossadtchi, A.; Mandelshtam, V. A.; Reisler, H. Reconstruction of Abel-Transformable Images: The Gaussian Basis-Set Expansion Abel Transform Method. *Rev. Sci. Instrum.* **2002**, *73* (7), 2634-2642

(69) Zarate, E.; Apell, P.; Echenique, P. M. Calculation of Low-Energy-Electron Lifetimes. *Phys. Rev. B* **1999**, *60* (4), 2326-2332

(70) Del Fatti, N.; Voisin, C.; Achermann, M.; Tzortzakis, S.; Christofilos, D.; Vallee, F. Nonequilibrium Electron Dynamics in Noble Metals. *Phys. Rev. B* **2000**, *61* (24), 16956-16966

(71) Ritchie, R. H.; Ashley, J. C. Interaction of Hot Electrons with a Free Electron Gas. *J. Phys. Chem. Solids* **1965**, *26* (12), 1689-1694

(72) Aeschlimann, M.; Bauer, M.; Pawlik, S.; Knorren, R.; Bouzerar, G.; Bennemann, K. H. Transport and Dynamics of Optically Excited Electrons in Metals. *Appl. Phys. A* **2000**, *71* (5), 485-491

(73) Cao, J.; Gao, Y.; Elsayed-Ali, H. E.; Miller, R. J. D.; Mantell, D. A. Femtosecond Photoemission Study of Ultrafast Electron Dynamics in Single-Crystal Au(111) Films. *Phys. Rev. B* **1998**, *58* (16), 10948-10952

(74) Watanabe, K.; Menzel, D.; Nilius, N.; Freund, H. J. Photochemistry on Metal Nanoparticles. *Chem. Rev.* **2006**, *106* (10), 4301-4320

(75) Manjavacas, A.; Liu, J. G.; Kulkarni, V.; Nordlander, P. Plasmon-Induced Hot Carriers in Metallic Nanoparticles. *ACS Nano* **2014**, *8* (8), 7630-7638

(76) Pettine, J.; Grubisic, A.; Nesbitt, D. J. Angle- and Momentum-Resolved Photoelectron Velocity Map Imaging Studies of Thin Au Film and Single Supported Au Nanoshells. *J. Phys. Chem. C* **2018**, *122* (7), 3970-3984

(77) Eppink, A. T. J. B.; Parker, D. H. Velocity Map Imaging of Ions and Electrons Using Electrostatic Lenses: Application in Photoelectron and Photofragment Ion Imaging of Molecular Oxygen. *Rev. Sci. Instrum.* **1997**, *68* (9), 3477-3484

(78) Johnson, P. B.; Christy, R. W. Optical Constants of Noble Metals. *Phys. Rev. B* **1972**, *6* (12), 4370-4379

(79) Mongin, D.; Maioli, P.; Burgin, J.; Langot, P.; Cottancin, E.; D'Addato, S.; Canut, B.; Treguer, M.; Crut, A.; Vallee, F.; et al. Ultrafast Electron-Lattice Thermalization in Copper and Other Noble Metal Nanoparticles. *J. Phys. Condens. Mat.* **2019**, *31* (8), 084001

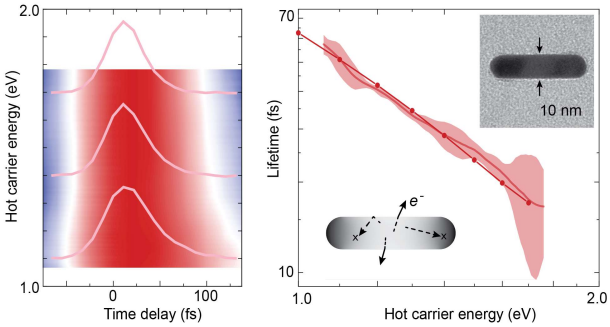

TOC Figure